



Refining Single-Atom Catalytic Kinetics for Tumor Homologous-Targeted Catalytic Therapy

Cite as

Nano-Micro Lett.

(2025) 17:253

Hengke Liu¹, Shan Lei¹, Hongyu Li¹, Jiayingzi Wu¹, Ting He¹, Jing Lin¹, Peng Huang¹ ✉

Received: 21 December 2024

Accepted: 16 March 2025

© The Author(s) 2025

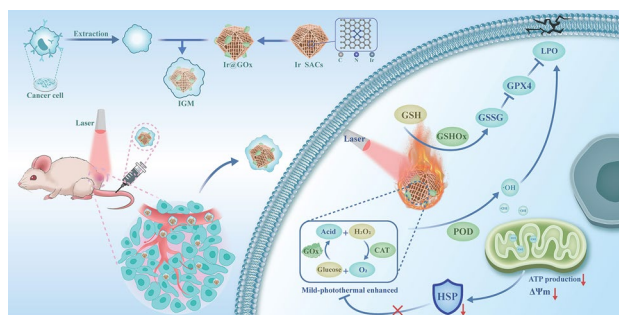
HIGHLIGHTS

- Developed a dual-enzyme cascade system integrating iridium single-atom nanozymes with glucose oxidase, optimizing hydrogen peroxide production, acidity, and temperature within the tumor microenvironment to markedly improve catalytic therapy efficacy.
- Functionalized the cascade reaction system with cancer cell membranes to achieve homologous targeting and high biocompatibility, ensuring accurate accumulation at tumor sites while minimizing off-target effects.

ABSTRACT Single-atom nanozymes (SAzymes) hold significant potential for tumor catalytic therapy, but their effectiveness is often compromised by low catalytic efficiency within tumor microenvironment. This efficiency is mainly influenced by key factors including hydrogen peroxide (H_2O_2) availability, acidity, and temperature. Simultaneous optimization of these key factors presents a significant challenge for tumor catalytic therapy. In this study, we developed a comprehensive strategy to refine single-atom catalytic kinetics for enhancing tumor catalytic therapy through dual-enzyme-driven cascade reactions.

Iridium (Ir) SAzymes with high catalytic activity and natural enzyme glucose oxidase (GOx) were utilized to construct the cascade reaction system. GOx was loaded by Ir SAzymes due to its large surface area. Then, the dual-enzyme-driven cascade reaction system was modified by cancer cell membranes for improving biocompatibility and achieving tumor homologous targeting ability. GOx catalysis reaction could produce abundant H_2O_2 and lower the local pH, thereby optimizing key reaction-limiting factors. Additionally, upon laser irradiation, Ir SAzymes could raise local temperature, further enhancing the catalytic efficiency of dual-enzyme system. This comprehensive optimization maximized the performance of Ir SAzymes, significantly improving the efficiency of catalytic therapy. Our findings present a strategy of refining single-atom catalytic kinetics for tumor homologous-targeted catalytic therapy.

KEYWORDS Single-atom nanozymes; Glucose oxidase; Biomimetic cascade catalysis; Tumor catalytic therapy; Mild-temperature photothermal therapy



Hengke Liu, Shan Lei, and Hongyu Li contributed have contributed equally.

✉ Peng Huang, peng.huang@szu.edu.cn

¹ Marshall Laboratory of Biomedical Engineering, Guangdong Key Laboratory for Biomedical Measurements and Ultrasound Imaging, Laboratory of Evolutionary Theranostics (LET), International Cancer Center, School of Biomedical Engineering, Shenzhen University Medical School, Shenzhen University, Shenzhen 518055, People's Republic of China

Published online: 12 May 2025



SHANGHAI JIAO TONG UNIVERSITY PRESS

Springer

1 Introduction

Tumor catalytic therapy, especially single-atom nanozymes (SAzymes)-mediated approaches, has emerged a research hot-spot in cancer treatment due to its ability to specifically generate reactive oxygen species (ROS) in tumor tissues [1–3]. The development of atomic nanotechnology has ushered in the era of SAzymes, which provide superior catalytic efficiency and customizable active sites, marking a great advancement over traditional nanoparticle-based catalysts [4, 5]. Recently, highly active SAzymes with well-defined metal–nitrogen–carbon (M–N–C, M = Mn, Fe, Co, Cu, Zn, Ru, etc.) coordination structures have been developed [6–11]. Notably, iridium (Ir) SAzyme demonstrates good biocompatibility and catalytic stability, making them promising candidates for tumor catalytic therapy [12, 13]. SAzyme-based catalytic therapy primarily focuses on regulating ROS level. Various strategies of improving SAzyme performance have been explored to enhance ROS yield, such as defect engineering [14, 15], doping with heterogeneous atoms [13], constructing near-neighbor monometallic atoms [16–19], or coupling with carriers [20–23]. The effectiveness of SAzyme-based therapies depends on both their catalytic activity and their adaptability to variations in the intratumoral microenvironment. Catalytic rates are influenced by factors such as temperature, pH, and hydrogen peroxide (H_2O_2) levels within tumor tissues [24–27]. Therefore, optimizing these parameters of catalytic process is crucial for efficient catalytic therapy.

In addition to optimizing catalytic kinetics, the development of an efficient delivery system is equally crucial. Current delivery systems for SAzyme encounter limitations, including low targeting efficiency, insufficient tumor accumulation and short blood circulation time. Recently, cancer cell membranes, as emerging biomimetic carriers, show great potential in the development of efficient delivery systems [28–30]. Cancer cell membrane-camouflaged nanoparticles retain key adhesion proteins, antigens, and membrane structures, preserving the surface characteristics and functions of the source cells [31, 32]. This approach enables homologous targeting, improved biocompatibility, extended blood circulation time, and enhanced cellular uptake compared to synthetic alternatives [28, 33]. Despite the significance of optimizing cascade reaction kinetics and enhancing tumor targeting, there have been limited studies exploring SAzyme-based cascade nanoreactors that can achieve high catalytic activity, sustained H_2O_2 supply,

reduced pH level, and heat generation—all of which are vital for effective tumor catalytic therapy.

Herein, we develop a strategy to comprehensively optimize the catalytic kinetics of SAzymes for traceable, multi-stage-enhanced catalytic therapy using a biomimetic cascade nanoreactor (Ir SAzymes@GOx@4T1M, IGM). The IGM was constructed by the combination of Ir SAzyme and natural enzyme glucose oxidase (GOx), followed by cancer cell membrane camouflage. The product H_2O_2 generated by GOx catalytic reaction can be used as the substrate of Ir SAzymes. Ir SAzymes-catalyzed reaction was optimized by producing H_2O_2 and reducing pH level through glucose oxidation reaction [34, 35]. Moreover, locally moderate heating further enhances the catalytic activity of both Ir SAzymes and GOx [36–39], yielding more cytotoxic hydroxyl radicals ($\cdot OH$). Meanwhile, Ir SAzymes also exhibit catalase (CAT)-like activity, breaking down H_2O_2 into O_2 , thus supporting the aerobic catalysis of GOx. Interestingly, the IGM exhibited high tumor accumulation through homotypic targeting of cell membrane camouflage. Ultimately, we comprehensively optimized the catalytic kinetics of Ir SAzymes and synchronously combined GOx, thus achieving dual-enzyme-driven cascade reactions and efficient catalytic therapy.

2 Experimental Section

2.1 Materials

$Ir(acac)_3$, $Zn(NO_3)_2 \cdot 6H_2O$, and glucose oxidase were obtained from Sigma-Aldrich (USA). 3,3',5,5'-tetramethylbenzidine (TMB) were purchased from Shanghai Macklin Biochemical Co., Ltd. 2',7'-Dichlorofluorescein diacetate (DCFH-DA), calcein-AM, propidium iodide (PI), enhanced BCA protein assay kit, Cell Counting Kit-8 (CCK-8), apoptosis detection kit (Annexin V-FITC/PI) and mitochondrial membrane potential assay kit with JC-1 were purchased from Beyotime Institute of Biotechnology (China). All the chemicals and solvents were used without further purification. Deionized water (18.2 M Ω cm) was used throughout the study.

2.2 Characterizations

Transmission electron microscopy (TEM) images were obtained using an HT7700 transmission electron microscope (Hitachi Electronics, accelerating voltage 80 kV). Elemental

mapping analysis was performed using a scanning transmission electron microscopy (JEM-3200FS, Tokyo, Japan) with an accelerating voltage of 300 kV. High-angle annular dark-field scanning transmission electron microscopy (HAADF-STEM) characterization was performed using a double spherical aberration-corrected transmission electron microscope (Titan Cubed Themis G2 300, Thermo Fisher, USA). X-ray powder diffraction (XRD) pattern was recorded in the 2θ range from 10° to 70° using a D8 Advance diffractometer (Bruker, Germany). The X-ray photoelectron spectroscopy (XPS) analysis was performed using ESCALAB 250Xi (Thermo Fisher, USA). Fourier-transform infrared (FT-IR) spectra were collected by an FT-IR spectrometer (Spectrum Two, PerkinElmer, USA) with the wavenumber range from 4000 to 400 cm^{-1} at 4 cm^{-1} resolution and 32 scans per sample. Zeta potential was measured using Zetasizer Nano-ZS90 (Malvern, England). The contents of Ir elements were measured using an inductively coupled plasma instrument (ICP-OES, Optima 7000DV, PerkinElmer, USA). UV/vis absorption spectra were measured using Cary 60 UV/vis spectrophotometer (Agilent Technologies, Santa Clara, CA, USA). Photoacoustic imaging images were obtained using an Vevo LAZR-X (VisualSonics Inc. New York, NY).

2.3 Synthesis of Ir SAzymes@GOx@4T1M (IGM)

Ir SAzymes was thoroughly ground and dispersed in water by sonication, and GOx was added to the Ir SAzymes solution at a 1:10 mass ratio of GOx to Ir SAzymes and stirred overnight. Free GOx was removed by centrifugation, and the resulting precipitates were collected to obtain Ir SAzymes@GOx. Next, 1 mg Ir SAzyme@GOx was mixed with an equal volume of 1 mg mL^{-1} (protein concentration) cell membrane vesicles in deionized water. The mixture was sonicated for 10 min using a bath sonicator, followed by centrifugation (10,000 rpm, 10 min) to collect Ir SAzymes@GOx@4T1M (IGM) which was then stored at 4°C for use. The cell membrane coating was then characterized by SDS-PAGE and TEM.

3 Results and Discussion

3.1 Preparation and Characterization of Ir SAzymes

Ir SAzymes were synthesized by the pyrolysis of Ir(acac)₃-loaded ZIF-8, resulting in a structure of single

Ir atom dispersed in nitrogen-doped carbon skeleton. During the pyrolysis process, the ZIF-8 framework prevented Ir atom aggregation. TEM and scanning electron microscopy (SEM) images revealed the rhombododecahedral structure of Ir(acac)₃@ZIF-8 nanocrystals (Fig. S1). High-resolution TEM (HRTEM) and high-angle annular dark-field scanning TEM (HAADF-STEM) images confirmed the absence of large Ir nanoparticles, while the distribution of single Ir atom was observed, as indicated by white circles (Fig. 1a, b). Element mapping images showed the uniform distribution of Ir, C, and N (Fig. 1c). Inductively coupled plasma atomic emission spectrometry (ICP-OES) quantified -0.39 wt\% Ir content in Ir SAzymes. As shown in X-ray diffraction (XRD) pattern, the broad peaks were assigned to amorphous graphitic carbon, without crystalline peaks of metallic Ir (Fig. S2). X-ray photoelectron spectroscopy (XPS) spectra identified pyrrolic N, pyridinic N, and graphitic N as anchoring sites for Ir atoms, ensuring single-atom dispersion (Fig. S3). X-ray absorption near-edge structure (XANES) analysis displayed the coordination environment of Ir atoms and showed absorption energies between metallic Ir and IrO₂, suggesting partially positive Ir atoms (Fig. 1d), which is consistent with Ir 4f XPS spectrum (Fig. 1e). Fourier-transformed extended X-ray absorption fine structure (FT-EXAFS) curves showed a peak at -1.6 \AA , indicating Ir-N coordination, with no Ir-Ir peak around 2.6 \AA , confirming isolated single Ir atom (Fig. 1f). EXAFS fitting curves indicated an average Ir-N bond length of 1.98 \AA (Table S1). Density functional theory (DFT) calculation identified most stable configuration as single Ir atom coordinated with four N atoms (Fig. 1g). Wavelet transform (WT) analysis further supported the FT-EXAFS results, showing maximum intensity at 5.1 \AA^{-1} for Ir-N coordination (Fig. 1h). Compared to WT plots of Ir powder and IrO₂, no Ir-Ir intensity was observed. These results confirmed the successful synthesis of Ir SAzymes.

3.2 Photothermal Property and Multienzyme Activities of Ir SAzymes

The Brunauer–Emmett–Teller (BET) measurement indicated that the Ir SAzymes exhibited a surface area of $821.3\text{ m}^2\text{ g}^{-1}$ and an average pore diameter of 8.9 nm , suggesting that the large surface area and porous structure benefit the exposure



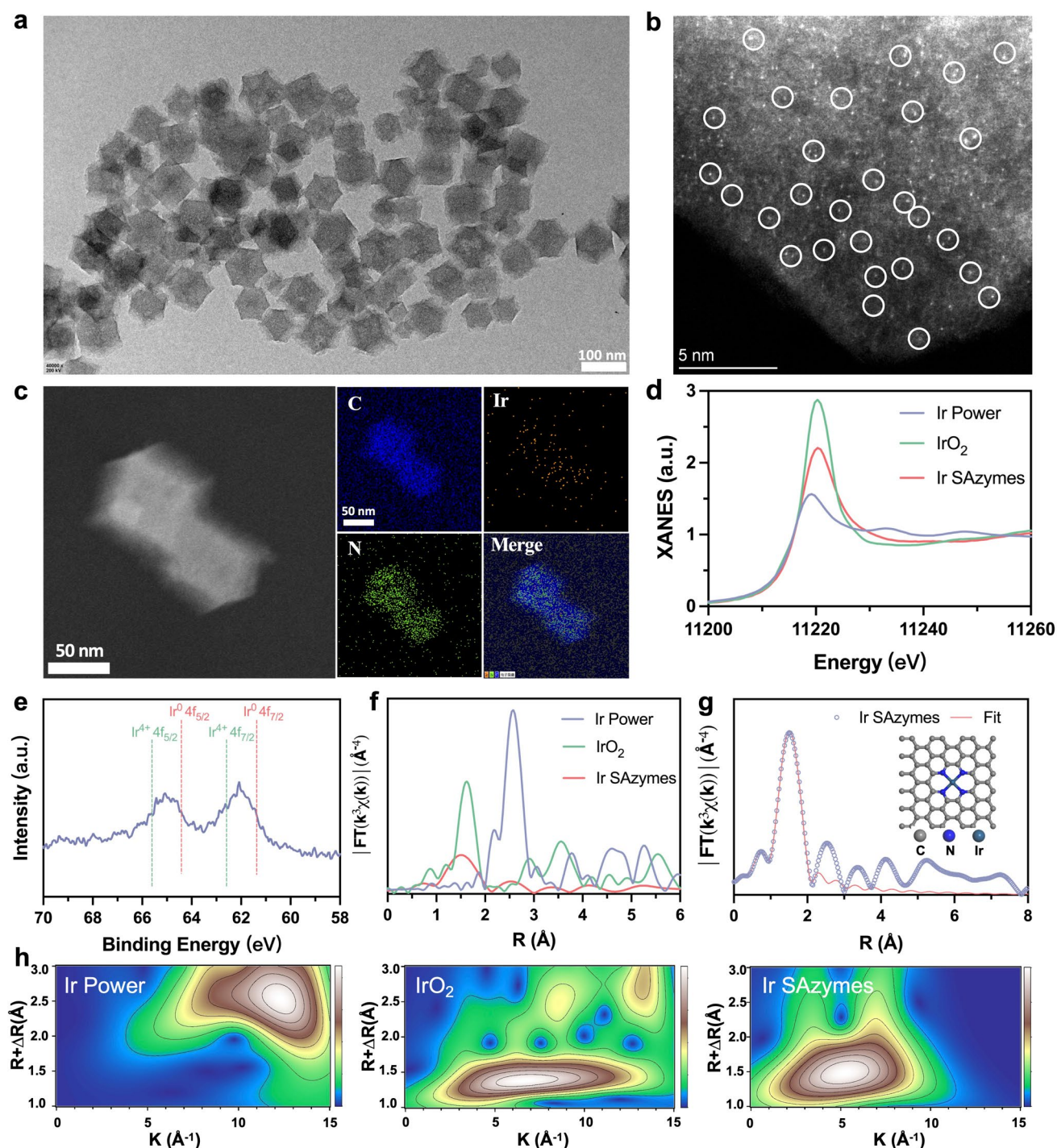


Fig. 1 Characterization of Ir SAzymes. **a** HRTEM, **b** Magnified HAADF-STEM image of Ir SAzymes. **c** Element mapping images of Ir SAzymes. **d** XANES of Ir powder, IrO₂, and Ir SAzymes at the Ir L_3 -edge. **e** XPS spectra of Ir SAzymes for Ir 4f regions. **f** FT-EXAFS spectra of Ir powder, IrO₂ and Ir SAzymes at the iridium L_3 -edge. **g** The corresponding R-space EXAFS fitting curves of Ir SAzymes. The inset illustrates the schematic model of the Ir SAzymes. **h** Wavelet transform plot of Ir L_3 -edge EXAFS of Ir powder, IrO₂, and Ir SAzymes

of single Ir active site and GOx loading (Figs. S4 and S5). The GOx loading capacity was calculated to be 1.7 wt%, as determined by the bicinchoninic acid (BCA) protein assay. According to the Arrhenius equation, the reaction rate constant increases exponentially with temperature, remarkably enhancing the catalytic reaction rate [40, 41]. The ultraviolet–visible–near infrared (UV–Vis–NIR) spectrum of Ir SAzymes revealed strong absorption in NIR region with an extinction coefficient of $5.46 \text{ L g}^{-1} \text{ cm}^{-1}$ at 808 nm (Fig. S6). Upon 808 nm laser irradiation, the temperature of the Ir SAzymes dispersion markedly increased in a concentration-dependent manner (Figs. 2a and S7). Ir SAzymes exhibited good photothermal stability and a photothermal conversion efficiency (PCE) of 38.1% (Fig. 2b, c).

The multienzyme mimetic activities of Ir SAzymes were further investigated. The CAT-like activity of Ir SAzymes in H_2O_2 decomposition was observed using confocal laser scanning microscopy (CLSM), visualizing the generation of O_2 bubbles. Experiments quantifying H_2O_2 consumption showed oxygen-generating capability of Ir SAzymes, especially under laser irradiation, indicating that the CAT-like activity could be enhanced by photothermal effect (Fig. 2d, e). The decomposition of H_2O_2 by Ir SAzymes follows by Michaelis–Menten kinetics equation with a K_m value of 49.41 mM (Fig. S8), which is equivalent to natural CAT (52.14 mM) [42]. A colorimetric reaction using 3,3',5,5'-tetramethylbenzidine dihydrochloride (TMB) followed Michaelis–Menten kinetics, with a Menten constant (K_m) of 23.74 mM and a maximum reaction rate (V_{\max}) of $2.89 \mu\text{M s}^{-1}$ (Figs. 2f, g and S9). Furthermore, laser irradiation increased TMB oxidation by 1.34-fold compared to the non-irradiated group (Fig. 2h). These findings indicated that laser irradiation enhanced both CAT-like and POD-like activities. According to the Arrhenius equation, the reaction rate constant increased exponentially with temperature, thus accelerating the catalytic rate. Therefore, the observed enhancement of enzyme activity is attributed to the photothermal effect. As shown in Fig. 2i, the decreased absorption intensity of 5-thio-2-nitrobenzoic acid (TNB) at 412 nm indicated the effective glutathione oxidase (GSHOx)-like activity of Ir SAzymes, which could further enhance tumor catalytic therapy.

To understand the catalytic mechanism and structure–activity relationship of Ir SAzymes, DFT calculations were performed. For POD-like activity, the H_2O_2 molecule initially adsorbs onto single Ir atoms on Ir SAzymes with

an adsorption energy of 0.069 eV (Fig. 2j, k). The dissociation of activated H_2O_2 could generate a reactive $\cdot\text{OH}$ and an attached hydroxyl group ($^*\text{OH}$) by the Ir site. Subsequently, the attached $^*\text{OH}$ reacted with a protonated hydrogen atom to produce H_2O . This process was accompanied by an obvious Gibbs free energy decrease (−1.08 eV). Hence, DFT analysis revealed that Ir SAzymes exhibited POD-like activity. For GSHOx-like activity, GSH molecule spontaneously adsorbed onto Ir atom and could be dissociated in the presence of O and OH groups from H_2O to form $^*\text{GS}$. The generated $^*\text{GS}$ subsequently coupled to form GSSG, the total Gibbs free energy decrease (−3.13 eV), indicating high GSHOx-like activity of Ir SAzymes (Fig. 2l, m).

3.3 Construction of the Dual-Enzyme-Driven Cascade Reaction Platform

To improve the biocompatibility and homologous targeting ability, cancer cell membranes nanovesicles (Fig. S10) derived from 4T1 cells were used to encapsulate Ir SAzymes through hydrophobic interactions [32, 43], producing cancer cell membrane-cloaked Ir SAzyme@GOx (IGM). TEM images showed a thick coating layer of 4T1 cell membrane surrounding the rhombododecahedron-shaped Ir SAzymes (Fig. 3a). The FT-IR analysis revealed that the composition of IGM is characterized by strong peaks corresponding to both GOx (1656 cm^{-1} , indicating C=O group) and 4T1M (1096 cm^{-1} , corresponding to the C-O-P group), confirming the formation of IGM composites (Fig. S11). After coating, the zeta potential of Ir SAzymes changed from 5.6 ± 1.1 to $-14.3 \pm 4.2 \text{ mV}$ (Fig. S12). SDS-PAGE analysis further confirmed the successful modification of 4T1 cell membranes (Fig. S13). DLS analysis indicated that the hydrodynamic size of Ir SAzymes was 196.6 nm, increasing to 226.3 nm after cell membrane coating, suggesting successful surface modification (Fig. S14a). In addition, IGM exhibited no obvious size change over seven days in various physiological solutions, verifying its good stability (Fig. S14b).

Encouraged by the high catalytic performance of SAzymes, in vitro anticancer activity of IGM was further assessed. The cytotoxicity of Ir SAzymes@Membrane (IM) was assessed against MCF-10A (normal cells) and 4T1 (tumor cells) using a Cell Counting Kit-8 (CCK-8) assay. The findings indicated negligible cytotoxic effects on MCF-10A cells, even at high concentrations, while 4T1 cell viability was significantly

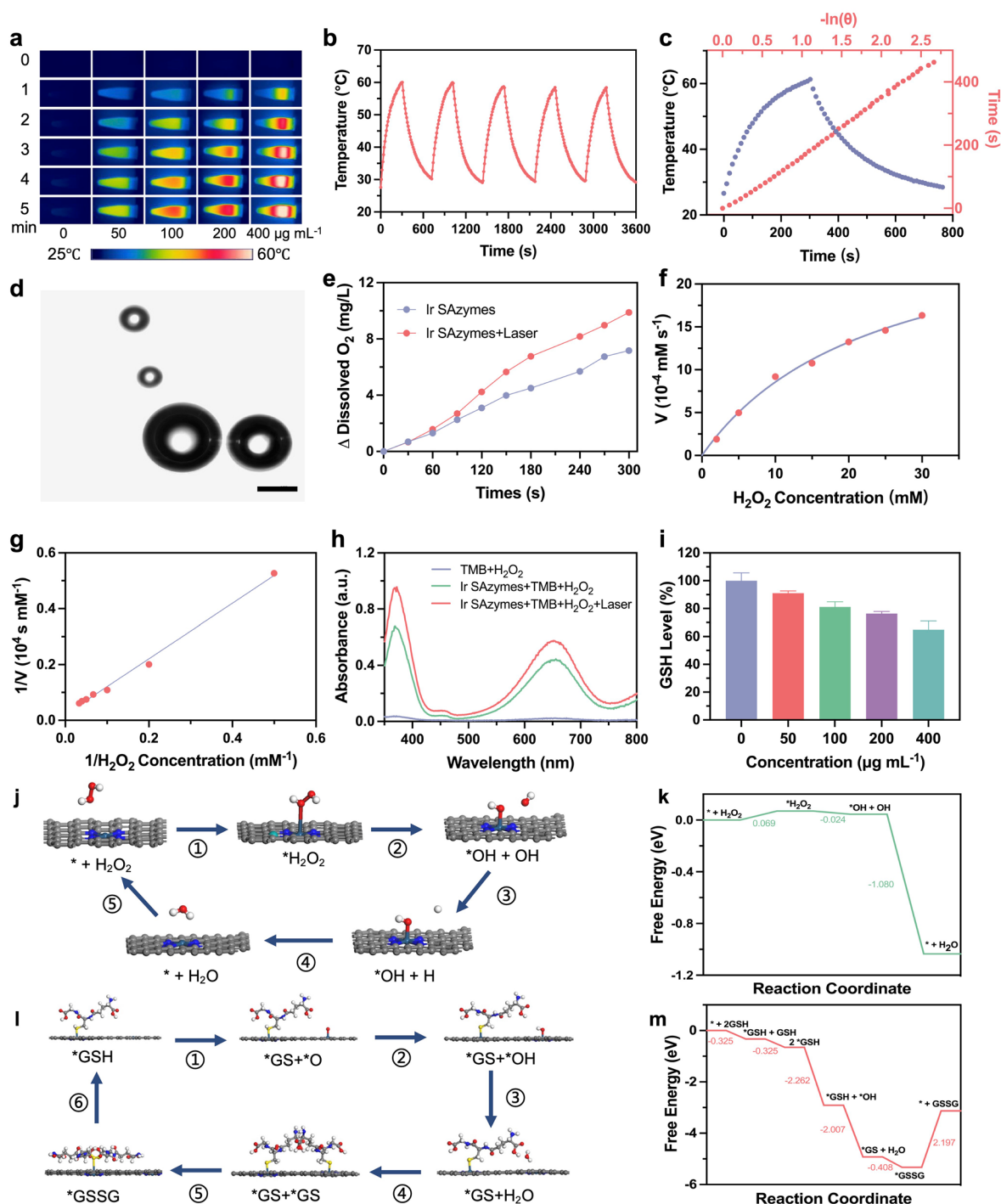


Fig. 2 **a** Thermal images of Ir SAzymes aqueous solutions under laser irradiation (808 nm, 0.8 W cm⁻²). **b** Photothermal stability of Ir SAzymes (400 μg mL⁻¹) under five successive laser on/off cycles. **c** PCE of Ir SAzymes. **d** Confocal microscopy images of O₂ bubbles in an Ir SAzymes and H₂O₂ mixture. Scale bar: 200 μm. **e** O₂ generation in various groups (pH=6.5). Ir SAzymes concentration: 50 μg mL⁻¹, H₂O₂ concentration: 1 mM. **f** Kinetic analysis of Ir SAzymes with POD-like activity. The concentration of H₂O₂ was varied in the presence of TMB (500 μM). **g** Double-reciprocal plots of Ir SAzymes activities derived from the Michaelis–Menten equation. **h** UV–Vis absorption spectra of TMB solution with and without 808 nm laser irradiation (0.8 W cm⁻², 3 min). **i** GSH depletion after incubation with different concentrations of Ir SAzymes. **j** Schematic illustration of the catalytic mechanism and **k** corresponding free energy diagrams of GSHox-like activity of Ir SAzymes. **l** Schematic illustration of the catalytic mechanism and **m** corresponding free energy diagrams of GSHox-like activity of Ir SAzymes. Cyan, blue, gray, red, white, and yellow spheres represent Ir, N, C, O, H, and S atoms, respectively

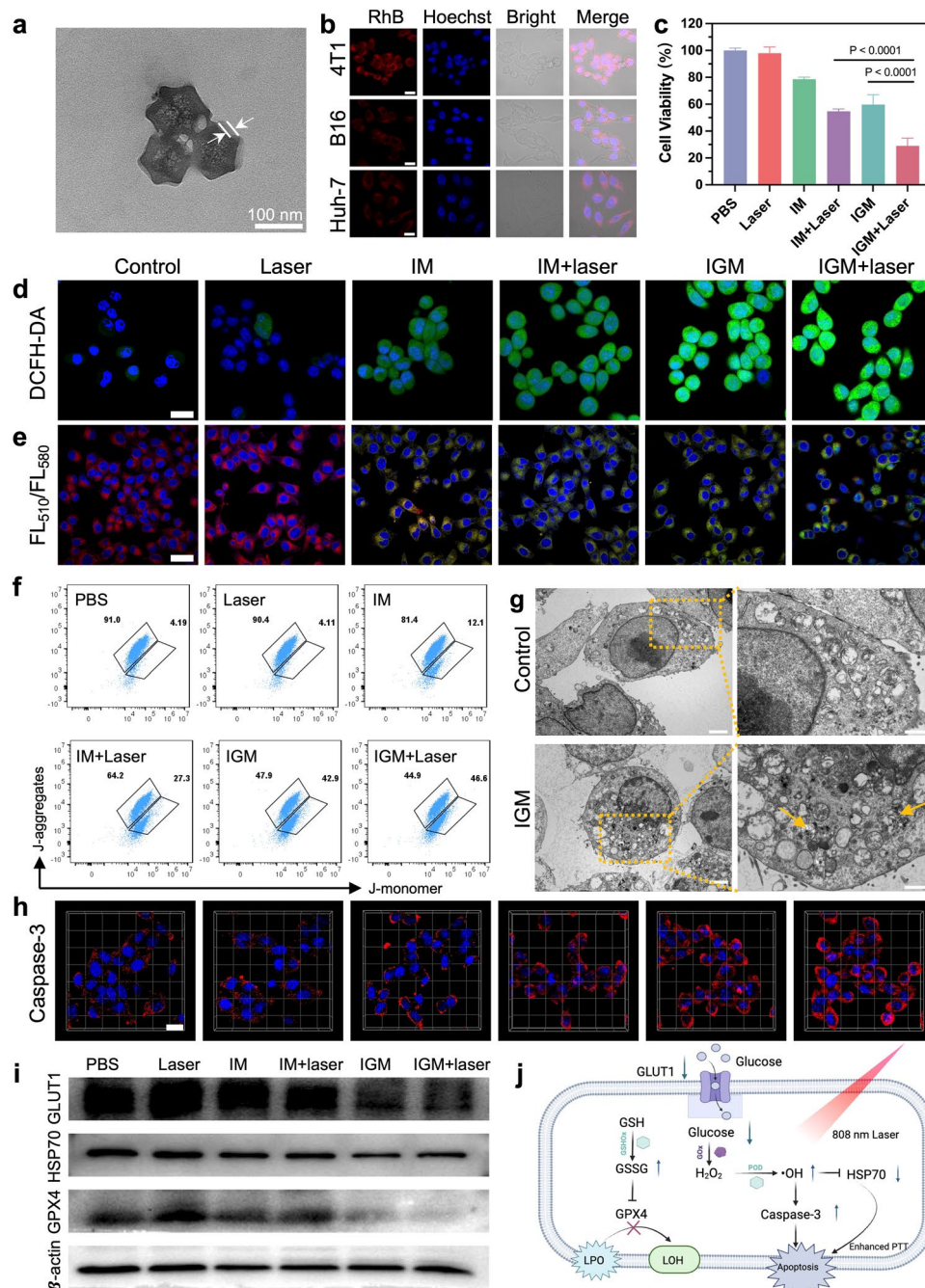


Fig. 3 **a** TEM images of the synthesized IGM. **b** Fluorescence images of various cells treated with RhB-labeled IGM, Scale bar: 20 μ m. **c** Cytotoxicity assessment of 4T1 cells with different treatments. **d** Confocal images of 4T1 cells stained with DCFH-DA, and **e** C11-BODIPY^{581/591} after various treatments. Scale bar: 20 μ m. **f** Flow cytometry analysis of the J-monomer and J-aggregates after various treatments. **g** Bio-TEM images of 4T1 cells with different treatments (orange arrow indicate the IGM; scale bars: 2 μ m and 1 μ m, respectively). **h** Confocal images of 4T1 cells stained with activation of caspase-3 after various treatments. Scale bar: 20 μ m. **i** Western blots of GLUT1, HSP70, and GPX4 after various treatments. **j** Potential antitumor mechanism of IGM plus laser-mediated catalytic therapy

reduced. This suggests that IM was selectively activated in an acidic environment (Fig. S15). Efficient uptake of SAzymes by tumor cells is crucial for effective tumor therapy. Flow

cytometry showed rapid IGM uptake by 4T1 cells with time-dependent fluorescence enhancement (Fig. S16). To verify homologous targeting, 4T1, B16, and Huh-7 cells were

incubated with Rhodamine B (RhB)-labeled IGM nanoparticles (RhB-IGM) and examined with CLSM (Fig. 3b, S17). The red fluorescence intensity in 4T1 cells was 2.4- and 2.7-fold higher than that of in B16 and Huh-7 cells, respectively, demonstrating its homologous targeting capability [28]. After verifying the effective cellular internalization provided by the 4T1 cell membrane camouflage, next, the *in vitro* cascade catalytic efficacy of IGM was evaluated. After treatment with IGM ($40\text{ }\mu\text{g mL}^{-1}$), 4T1 cell viability decreased by 40.2%, whereas IM alone exhibited mild toxicity (21.3%) (Fig. 3c). Upon 808 nm laser irradiation for 5 min, IGM treatment exhibited obvious cytotoxicity, suggesting the dual-enzyme-driven cascade reaction could be enhanced by photothermal effect. Flow cytometry analysis with Annexin V and propidium iodide (PI) co-staining also confirmed the highest apoptosis rate in the IGM plus laser group (Figs. S18 and S19).

3.4 In Vitro Enhanced Catalytic Therapy of IGM

To further elucidate the mechanism of cell death, we studied the variation of intracellular molecular events associated with the cascade reaction. The obvious fluorescence signal of 2',7'-dichlorofluorescein diacetate (DCFH-DA) in IGM treatment group showed that the IGM could induce ROS generation, which was further enhanced by laser irradiation (Figs. 3d and S20). ROS accumulation plays a pivotal role in lipid peroxidation (LPO) of cell membranes and DNA damage, ultimately inducing cell death [44, 45]. LPO was evaluated using the ratiometric fluorescent probe C11-BODIPY^{581/591}. The IGM + Laser treatment group exhibited a strong green fluorescence signal and a weak red signal, indicating enhanced ROS generation and subsequent LPO under laser irradiation (Fig. 3e). Alterations in mitochondrial membrane potential (MMP) were assessed using the JC-1 fluorescent probe and showed that the ratio of JC-1 monomers (low MMP) in the IGM-treated group (42.9%) was 3.54-fold higher than that of in the IM-treated group (12.1%), suggesting the mitochondrial depolarization by cascade catalysis (Fig. 3f). Additionally, IGM treatment resulted in the lower adenosine triphosphate (ATP) levels in tumor cells, suggesting mitochondrial dysfunction (Fig. S21). The ROS-related cytotoxicity of IGM was further confirmed through bio-TEM imaging. Reduced cell size and nuclear chromatin condensation, hallmarks of apoptosis,

were observed in cells treated with IGM (Fig. 3g). Upon laser irradiation, IGM induced significant cell apoptosis, as demonstrated by the elevated expression of caspase-3 (Figs. 3h and S22). Subsequently, the combined therapeutic molecular mechanism was investigated. Glucose transporter 1 (GLUT1) is a glucose transporter protein that is upregulated and promotes tumor cell growth and survival [46]. Notably, GLUT1 expression was down-regulated in cells treated with IGM, and further reduced by laser irradiation (Figs. 3i and S23). IGM treatment led to obvious down-regulation of HSP70, suggesting ROS inhibition of heat shock proteins (HSPs) [47, 48]. The IGM treatment showed LPO accumulation and reduced glutathione peroxidase 4 (GPX4) expression, illustrating GPX4 inactivation along with GSH consumption. Figure 3j summarizes the potential molecular mechanisms underlying IGM-mediated catalytic therapy. Our study revealed that the combination of IGM and laser irradiation effectively reduces ATP levels, increases $\cdot\text{OH}$ levels, downregulates GLUT1, GPX4, and HSP70, and activates caspase-3, thereby efficiently promoting cell apoptosis. These results suggest that optimizing the catalytic kinetics of the dual-enzyme system involves multiple molecular events within live cells, coupled with feedback mechanisms that synergistically enhanced tumor treatment efficacy.

3.5 In Vitro and In Vivo Imaging

Inspired by the promising *in vitro* therapeutic effects of IGM, we conducted its antitumor effects *in vivo*. Initially, the accumulation of IGM at the tumor site was investigated to determine the optimal time window for laser-enhanced catalytic therapy. As a powerful imaging technique, photoacoustic (PA) imaging noninvasively and precisely traces the distribution of accumulated nanoparticles at the tumor site with high resolution [49, 50]. Given the photothermal properties of Ir SAzymes under laser irradiation, we evaluated the PA imaging potential of IGM both *in vitro* and *in vivo*. As shown in Fig. 4a, a clear PA signal proportional to the concentration of IGM was observed, suggesting that IGM could act as a PA contrast agent. For *in vivo* PA imaging, the IGM was administered via intravenous injection into 4T1 tumor-bearing mice. The PA signal intensity increased approximately 2.47-fold at 8-h post-injection compared to the initial signal at 0 h (Fig. 4b, c), suggesting that

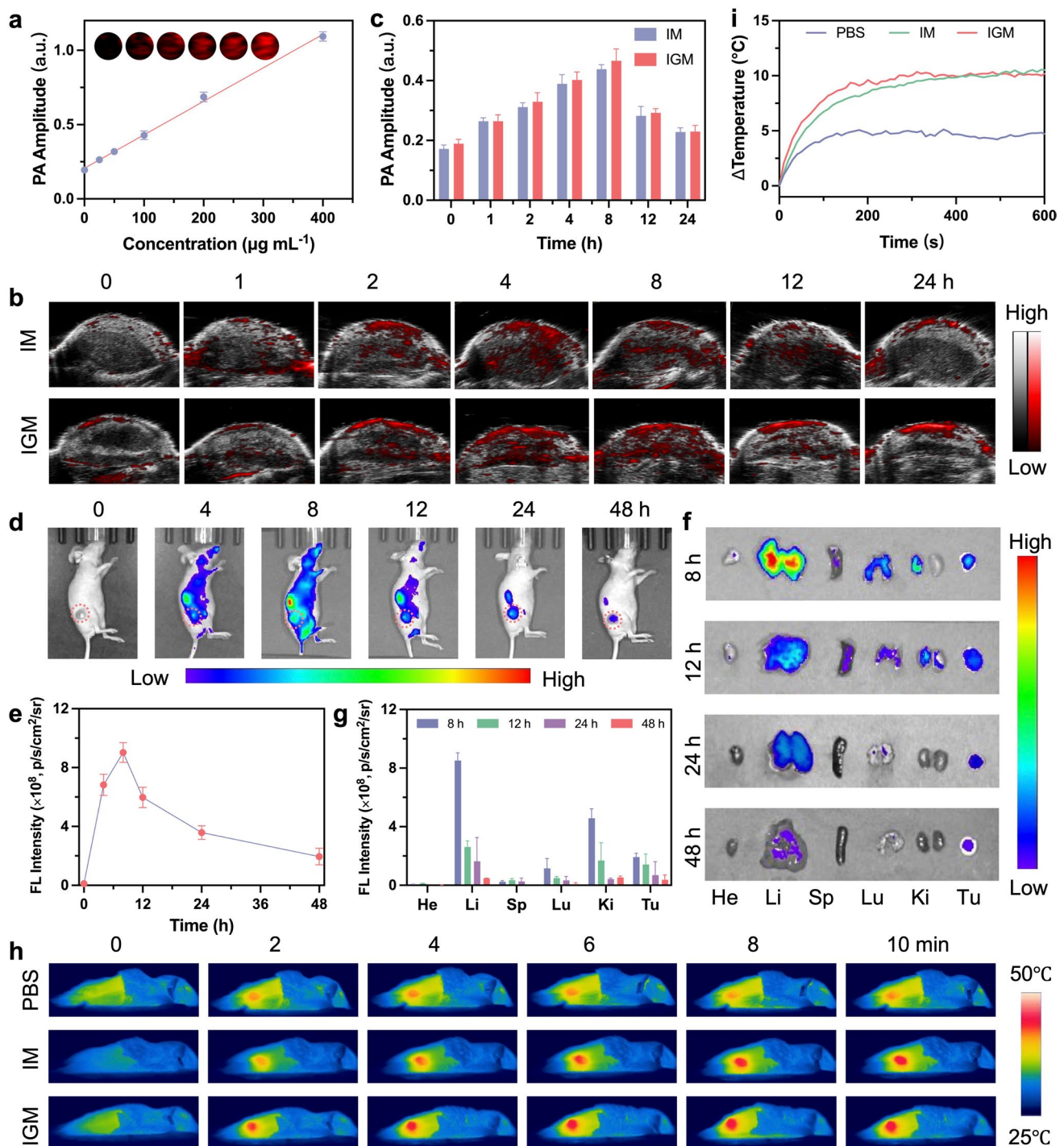


Fig. 4 **a** PA images and corresponding PA values at various IGM solution concentrations under 808 nm laser irradiation. **b** In vivo PA images and **c** quantification of PA amplitudes at tumor sites after *i.v.* injection of IM and IGM, presented as mean \pm SD ($n=3$). **d** Representative fluorescence images and **e** corresponding fluorescence intensity of tumor in mice at various time points after *i.v.* injection of IGM. **f** Representative fluorescence images of dissected organs and tumors at 8, 12, 24, and 48 h after injection of IGM-IR800, and **g** corresponding fluorescence intensity of major organs and tumor tissues. Data are presented as mean \pm SD ($n=3$). **h** Thermal images of mice after *i.v.* injection of PBS, IM, and IGM (808 nm, 0.8 W cm⁻², 10 min) and **i** corresponding changes in tumor temperature

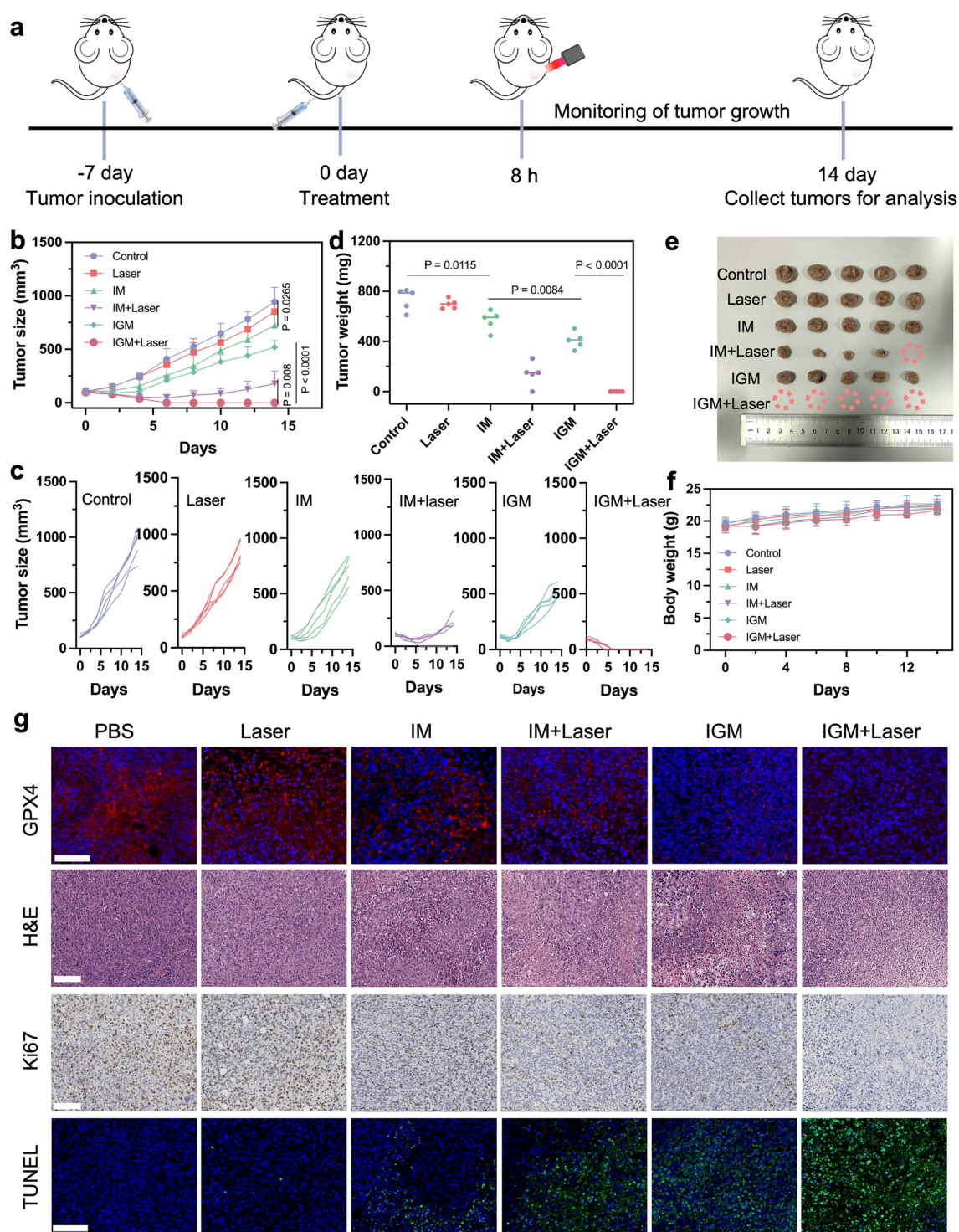


Fig. 5 **a** Treatment protocol for the antitumor experiment on 4T1 tumor-bearing mice. **b** Tumor growth curves after the indicated treatments, presented as mean \pm SD ($n=5$). **c** Individual tumor growth curves for each group after various treatments. **d** Tumor weight of mice after the indicated treatments. **e** Photographs of xenograft tumors excised from mice after 14 days of treatment. **f** Average body weight of mice throughout the indicated treatments. **g** GPX4, H&E, Ki67, and TUNEL staining images of tumor sections following various treatments. Scale bar: 100 μm

IGM could efficiently accumulate at the tumor site through homologous targeting. To track the metabolic behavior of IGM, we labeled IGM with a near infrared dye, IRdye 800CW NHS ester (IR800), for *in vivo* fluorescence imaging. Following intravenous injection of IGM-IR800, the fluorescence intensity of the tumor reached its peak at 8 h and remained elevated up to 48 h. This prolonged signal indicates that the cancer cell membrane camouflage effectively maintained high enrichment of IGM in the tumor tissue (Fig. 4d, e). Additionally, mice were sacrificed at various time points (8, 12, 24, and 48 h), and major organs and tumors were harvested to quantify the distribution of IGM (Fig. 4f, g). Fluorescence images of major organs revealed that IGM was primarily metabolized by the liver and kidneys. Furthermore, to investigate the pharmacokinetic profile of IGM in 4T1 tumor-bearing mice, blood samples were collected at different time intervals post-injection to assess drug concentrations. The blood half-life of IGM was found to be 4.14 ± 1.56 h (Fig. S24, Table S2), which contributes to improved tumor accumulation and therapeutic potential. Next, we evaluated the *in vivo* therapeutic efficacy of IGM in a 4T1 tumor-bearing mouse model. We firstly performed *in vivo* photothermal imaging to assess the generation of localized hyperthermia. Compared to the PBS group, IGM-treated mice exhibited a rapid temperature increase within the tumor region under 808 nm laser irradiation, with the maximum temperature reaching 45.2 °C within 10 min (Fig. 4h, i).

3.6 In Vivo Enhanced Catalytic Therapy of IGM

After that, the *in vivo* antitumor effect of IGM was evaluated in 4T1 tumor-bearing mice. The 4T1 tumor-bearing mice were randomly divided into six groups ($n=5$ per group): Control (PBS), Laser, IM, IM + Laser, IGM, and IGM + Laser. Detailed methodologies for the construction of the mouse model and subsequent interventions are presented in Fig. 5a. Tumor growth curves showed that PBS or laser treatment alone exhibited negligible inhibition effect on tumors. In contrast, IGM showed superior catalytic therapeutic efficacy compared to IM, which was further enhanced by laser irradiation, underscoring the robust *in vivo* cascade catalytic therapeutic efficacy of IGM (Fig. 5b, c). Individual tumor growth curves and photographs of excised tumors showed complete tumor clearance in the IGM + Laser group,

demonstrating the effectiveness of the fully optimized single-atom catalytic therapy (Fig. 5d, e). During the treatment period, all mouse groups showed a slight increase in body weight (Fig. 5f). Additionally, immunofluorescence imaging revealed a significant reduction in GPX4 and HSP70 expression levels, attributed to the IGM-induced ferroptosis response (Figs. 5g, S25 and S26). To further investigate the antitumor efficacy of IGM, tumor sections from different groups were stained with hematoxylin and eosin (H&E), Ki-67, and TdT-mediated dUTP nick-end labeling (TUNEL) for histological analysis (Figs. 5g and S27). The IGM + Laser group showed the most significant cell damage and the highest apoptotic cell population, underscoring the strong therapeutic potential of this optimized single-atom catalytic therapy *in vivo*. Importantly, hemolysis and blood biochemistry analysis (Figs. S28 and S29) demonstrated the good biocompatibility of IGM. Meanwhile, the H&E staining images of major organs showed no inflammation or obvious tissue damage (Fig. S30), collectively confirming the good biocompatibility of IGM for *in vivo* theranostic applications. Collectively, these experimental results indicated that IGM exhibited effective antitumor effect and good biocompatibility, offering a promising strategy to enhance single-atom nanozyme-mediated catalytic therapy.

4 Conclusion

In summary, we developed an optimized strategy to enhance single-atom catalytic kinetics for traceable, multistage catalytic therapy using a biomimetic cascade nanoreactor (IGM). By leveraging cancer cell membrane camouflage, IGM effectively targeted tumors, with substantial tumor accumulation confirmed through *in vivo* PA imaging. GOx-assisted catalysis intensified the intratumoral catalytic process of Ir SAzymes by further acidifying the tumor microenvironment and increasing H₂O₂ availability, thereby facilitating ·OH radical generation. By further enhancing the catalytic rate of dual-enzyme system through laser irradiation, IGM show good therapeutic potential both *in vitro* and *in vivo*. This study addresses the key limitations of tumor catalytic therapy, including inadequate tumor targeting, low catalytic efficiency, and insufficient H₂O₂ availability within the tumor microenvironment. Consequently, this strategy offers a promising pathway to enhance intratumoral catalytic



kinetics and improve the efficacy of SAzymes-mediated tumor catalytic therapy.

Acknowledgements This work is financially supported by National Natural Science Foundation of China (U23A2097, 82372116, 22474079, 22104094, 82302362), Shenzhen Medical Research Fund (B2302047), Basic Research Program of Shenzhen (KQTD20190929172538530, JCYJ20220818095806014, JCYJ20240813142810014), Natural Science Foundation of Guangdong Province (2024A1515012677), Research Team Cultivation Program of Shenzhen University (2023QNT017, 2023QNT019), and Shenzhen University 2035 Program for Excellent Research (2024C004). We thank the Instrumental Analysis Center of Shenzhen University.

Authors' Contributions All authors agreed to all the contents of the manuscript. Hengke Liu, Shan Lei, and Hongyu Li contributed equally to this work as co-first authors. Hengke Liu, Shan Lei, and Hongyu Li were involved in data curation, investigation, methodology, visualization, and writing of the original draft. Jiayingzi Wu and Ting He were involved in methodology, formal analysis, and investigation. Jing Lin was involved in supervision, methodology, formal analysis, and investigation. Peng Huang was involved in supervision, funding acquisition, and writing—reviewing and editing.

Declarations

Conflict of Interest The authors declare no competing financial interest. They have no known competing financial interests or personal relationships that could have appeared to influence the work reported in this paper.

Supporting Information Some details of cell and animal experiments, additional results including XRD pattern, Cell uptake, photographs of the experimental process, H&E staining images of normal tissues, and other additional information.

Open Access This article is licensed under a Creative Commons Attribution 4.0 International License, which permits use, sharing, adaptation, distribution and reproduction in any medium or format, as long as you give appropriate credit to the original author(s) and the source, provide a link to the Creative Commons licence, and indicate if changes were made. The images or other third party material in this article are included in the article's Creative Commons licence, unless indicated otherwise in a credit line to the material. If material is not included in the article's Creative Commons licence and your intended use is not permitted by statutory regulation or exceeds the permitted use, you will need to obtain permission directly from the copyright holder. To view a copy of this licence, visit <http://creativecommons.org/licenses/by/4.0/>.

Supplementary Information The online version contains supplementary material available at <https://doi.org/10.1007/s40820-025-01735-y>.

References

1. S. Lei, J. Zhang, N.T. Blum, M. Li, D.-Y. Zhang et al., *In vivo* three-dimensional multispectral photoacoustic imaging of dual enzyme-driven cyclic cascade reaction for tumor catalytic therapy. *Nat. Commun.* **13**(1), 1298 (2022). <https://doi.org/10.1038/s41467-022-29082-1>
2. H. Lin, Y. Chen, J. Shi, Nanoparticle-triggered *in situ* catalytic chemical reactions for tumour-specific therapy. *Chem. Soc. Rev.* **47**(6), 1938–1958 (2018). <https://doi.org/10.1039/c7cs00471k>
3. H. Xiang, W. Feng, Y. Chen, Single-atom catalysts in catalytic biomedicine. *Adv. Mater.* **32**(8), e1905994 (2020). <https://doi.org/10.1002/adma.201905994>
4. H. Zhang, X.F. Lu, Z.P. Wu, X.W.D. Lou, Emerging multifunctional single-atom catalysts/nanozymes. *ACS Cent. Sci.* **6**(8), 1288–1301 (2020). <https://doi.org/10.1021/acscentsci.0c00512>
5. Y. Liu, H. Zhao, Y. Zhao, Designing efficient single metal atom biocatalysts at the atomic structure level. *Angew. Chem. Int. Ed.* **63**(13), e202315933 (2024). <https://doi.org/10.1002/anie.202315933>
6. S. Cai, J. Liu, J. Ding, Z. Fu, H. Li et al., Tumor-microenvironment-responsive cascade reactions by a cobalt-single-atom nanozyme for synergistic nanocatalytic chemotherapy. *Angew. Chem. Int. Ed.* **61**(48), e202204502 (2022). <https://doi.org/10.1002/anie.202204502>
7. Y. Zhu, W. Wang, J. Cheng, Y. Qu, Y. Dai et al., Stimuli-responsive manganese single-atom nanozyme for tumor therapy via integrated cascade reactions. *Angew. Chem. Int. Ed.* **60**(17), 9480–9488 (2021). <https://doi.org/10.1002/anie.202017152>
8. S. Ji, B. Jiang, H. Hao, Y. Chen, J. Dong et al., Matching the kinetics of natural enzymes with a single-atom iron nanozyme. *Nat. Catal.* **4**(5), 407–417 (2021). <https://doi.org/10.1038/s41929-021-00609-x>
9. Z. Zhao, H. Tan, P. Zhang, X. Liang, T. Li et al., Turning the inert element zinc into an active single-atom catalyst for efficient Fenton-like chemistry. *Angew. Chem. Int. Ed.* **62**(18), e202219178 (2023). <https://doi.org/10.1002/anie.202219178>
10. D. Wang, J. Wang, X.J. Gao, H. Ding, M. Yang et al., Employing noble metal-porphyrins to engineer robust and highly active single-atom nanozymes for targeted catalytic therapy in nasopharyngeal carcinoma. *Adv. Mater.* **36**(7), e2310033 (2024). <https://doi.org/10.1002/adma.202310033>
11. M. Chang, Z. Hou, M. Wang, D. Wen, C. Li et al., Cu single atom nanozyme based high-efficiency mild photothermal therapy through cellular metabolic regulation. *Angew. Chem. Int. Ed.* **61**(50), e202209245 (2022). <https://doi.org/10.1002/anie.202209245>
12. Z. Wang, W. Wang, J. Wang, D. Wang, M. Liu et al., Single-atom catalysts with ultrahigh catalase-like activity through electron filling and orbital energy regulation. *Adv. Funct. Mater.* **33**(2), 2209560 (2023). <https://doi.org/10.1002/adfm.202209560>

13. Y. Liu, B. Wang, J. Zhu, X. Xu, B. Zhou et al., Single-atom nanozyme with asymmetric electron distribution for tumor catalytic therapy by disrupting tumor redox and energy metabolism homeostasis. *Adv. Mater.* **35**(9), e2208512 (2023). <https://doi.org/10.1002/adma.202208512>
14. B. Yu, W. Wang, W. Sun, C. Jiang, L. Lu, Defect engineering enables synergistic action of enzyme-mimicking active centers for high-efficiency tumor therapy. *J. Am. Chem. Soc.* **143**(23), 8855–8865 (2021). <https://doi.org/10.1021/jacs.1c03510>
15. J. Liu, B. Yu, M. Rong, W. Sun, L. Lu, A new strategy to fight tumor heterogeneity: Integrating metal-defect active centers within NADH oxidase nanozymes. *Nano Today* **54**, 102113 (2024). <https://doi.org/10.1016/j.nantod.2023.102113>
16. Y. Liu, R. Niu, R. Deng, S. Song, Y. Wang et al., Multi-enzyme co-expressed dual-atom nanozymes induce cascade immunogenic ferroptosis *via* activating interferon- γ and targeting arachidonic acid metabolism. *J. Am. Chem. Soc.* **145**(16), 8965–8978 (2023). <https://doi.org/10.1021/jacs.2c13689>
17. R. Zeng, Q. Gao, L. Xiao, W. Wang, Y. Gu et al., Precise tuning of the D-band center of dual-atomic enzymes for catalytic therapy. *J. Am. Chem. Soc.* **146**(14), 10023–10031 (2024). <https://doi.org/10.1021/jacs.4c00791>
18. R. Zeng, Y. Li, X. Hu, W. Wang, Y. Li et al., Atomically site synergistic effects of dual-atom nanozyme enhances peroxidase-like properties. *Nano Lett.* **23**(13), 6073–6080 (2023). <https://doi.org/10.1021/acs.nanolett.3c01454>
19. G. Li, H. Liu, T. Hu, F. Pu, J. Ren et al., Dimensionality engineering of single-atom nanozyme for efficient peroxidase-mimicking. *J. Am. Chem. Soc.* **145**(30), 16835–16842 (2023). <https://doi.org/10.1021/jacs.3c05162>
20. J. Yang, H. Yao, Y. Guo, B. Yang, J. Shi, Enhancing tumor catalytic therapy by co-catalysis. *Angew. Chem. Int. Ed.* **61**(17), e202200480 (2022). <https://doi.org/10.1002/anie.202200480>
21. G. Feng, H. Huang, M. Zhang, Z. Wu, D. Sun et al., Single atom iron-doped graphitic-phase C_3N_4 semiconductor nanosheets for augmented sonodynamic melanoma therapy synergy with endowed chemodynamic effect. *Adv. Sci.* **10**(23), e2302579 (2023). <https://doi.org/10.1002/advs.202302579>
22. J. Zhou, D. Xu, G. Tian, Q. He, X. Zhang et al., Coordination-driven self-assembly strategy-activated Cu single-atom nanozymes for catalytic tumor-specific therapy. *J. Am. Chem. Soc.* **145**(7), 4279–4293 (2023). <https://doi.org/10.1021/jacs.2c13597>
23. H. Yang, M. Luo, S. Lu, Q. Zhang, Y. Chao et al., Low-temperature aerobic oxidation of thiophenic sulfides over atomic Mo hosted by cobalt hydroxide sub-nanometer sheets. *Chem* **8**(9), 2460–2471 (2022). <https://doi.org/10.1016/j.chempr.2022.06.001>
24. W. He, J. Wu, J. Liu, J. Li, Single-atom nanozymes for catalytic therapy: recent advances and challenges. *Adv. Funct. Mater.* **34**(16), 2312116 (2024). <https://doi.org/10.1002/adfm.202312116>
25. C. Peng, R. Pang, J. Li, E. Wang, Current advances on the single-atom nanozyme and its bioapplications. *Adv. Mater.* **36**(10), e2211724 (2024). <https://doi.org/10.1002/adma.202211724>
26. J. Liu, A. Wang, S. Liu, R. Yang, L. Wang et al., A titanium nitride nanozyme for pH-responsive and irradiation-enhanced cascade-catalytic tumor therapy. *Angew. Chem. Int. Ed.* **60**(48), 25328–25338 (2021). <https://doi.org/10.1002/anie.202106750>
27. L. Yang, S. Dong, S. Gai, D. Yang, H. Ding et al., Deep insight of design, mechanism, and cancer theranostic strategy of nanozymes. *Nano-Micro Lett.* **16**(1), 28 (2023). <https://doi.org/10.1007/s40820-023-01224-0>
28. J. Cui, F. Zhang, D. Yan, T. Han, L. Wang et al., “Trojan horse” phototheranostics: fine-engineering NIR-II AIEgen camouflaged by cancer cell membrane for homologous-targeting multimodal imaging-guided phototherapy. *Adv. Mater.* **35**(33), 2302639 (2023). <https://doi.org/10.1002/adma.202302639>
29. B. Geng, J. Hu, Y. Li, S. Feng, D. Pan et al., Near-infrared phosphorescent carbon dots for sonodynamic precision tumor therapy. *Nat. Commun.* **13**(1), 5735 (2022). <https://doi.org/10.1038/s41467-022-33474-8>
30. Z. Liu, L. Zhang, T. Cui, M. Ma, J. Ren et al., A nature-inspired metal-organic framework discriminator for differential diagnosis of cancer cell subtypes. *Angew. Chem. Int. Ed.* **60**(28), 15436–15444 (2021). <https://doi.org/10.1002/anie.202102286>
31. M. Liu, Y. Feng, Y. Lu, R. Huang, Y. Zhang et al., Lymph-targeted high-density lipoprotein-mimetic nanovaccine for multi-antigenic personalized cancer immunotherapy. *Sci. Adv.* **10**(11), eadk2444 (2024). <https://doi.org/10.1126/sciadv.adk2444>
32. R.H. Fang, W. Gao, L. Zhang, Targeting drugs to tumours using cell membrane-coated nanoparticles. *Nat. Rev. Clin. Oncol.* **20**(1), 33–48 (2023). <https://doi.org/10.1038/s41571-022-00699-x>
33. Y. Zou, Y. Sun, Y. Wang, D. Zhang, H. Yang et al., Cancer cell-mitochondria hybrid membrane coated Gboxin loaded nanomedicines for glioblastoma treatment. *Nat. Commun.* **14**(1), 4557 (2023). <https://doi.org/10.1038/s41467-023-40280-3>
34. L.-H. Fu, C. Qi, J. Lin, P. Huang, Catalytic chemistry of glucose oxidase in cancer diagnosis and treatment. *Chem. Soc. Rev.* **47**(17), 6454–6472 (2018). <https://doi.org/10.1039/c7cs00891k>
35. L.H. Fu, C. Qi, Y.R. Hu, J. Lin, P. Huang, Glucose oxidase-instructed multimodal synergistic cancer therapy. *Adv. Mater.* **31**(21), 1808325 (2019). <https://doi.org/10.1002/adma.201808325>
36. J. Wu, Y. Zhang, K. Jiang, X. Wang, N.T. Blum et al., Enzyme-engineered conjugated polymer nanoplatfor for activatable companion diagnostics and multistage augmented synergistic therapy. *Adv. Mater.* **34**(18), e2200062 (2022). <https://doi.org/10.1002/adma.202200062>
37. T. He, H. Xu, Y. Zhang, S. Yi, R. Cui et al., Glucose oxidase-instructed traceable self-oxygenation/hyperthermia dually enhanced cancer starvation therapy. *Theranostics* **10**(4), 1544–1554 (2020). <https://doi.org/10.7150/thno.40439>



38. C. Yang, M.R. Younis, J. Zhang, J. Qu, J. Lin et al., Programmable NIR-II photothermal-enhanced starvation-primed chemodynamic therapy using glucose oxidase-functionalized ancient pigment nanosheets. *Small* **16**(25), e2001518 (2020). <https://doi.org/10.1002/sml.202001518>
39. X. Zhang, X. Chen, Y. Zhao, Nanozymes: versatile platforms for cancer diagnosis and therapy. *Nano-Micro Lett.* **14**(1), 95 (2022). <https://doi.org/10.1007/s40820-022-00828-2>
40. J. Kohout, Modified Arrhenius equation in materials science, chemistry and biology. *Molecules* **26**(23), 7162 (2021). <https://doi.org/10.3390/molecules26237162>
41. M. Zandieh, J.W. Liu, Nanozymes: Definition, activity, and mechanisms. *Adv. Mater.* **36**, 2211041 (2024). <https://doi.org/10.1002/adma.202211041>
42. R. Zhang, B. Xue, Y. Tao, H. Zhao, Z. Zhang et al., Edge-site engineering of defective Fe-N₄ nanozymes with boosted catalase-like performance for retinal vasculopathies. *Adv. Mater.* **34**(39), e2205324 (2022). <https://doi.org/10.1002/adma.202205324>
43. J. Cheng, L. Li, D. Jin, Y. Dai, Y. Zhu et al., Boosting ferroptosis therapy with iridium single-atom nanocatalyst in ultralow metal content. *Adv. Mater.* **35**(17), e2210037 (2023). <https://doi.org/10.1002/adma.202210037>
44. Q. Hu, W. Zhu, J. Du, H. Ge, J. Zheng et al., A GPX4-targeted photosensitizer to reverse hypoxia-induced inhibition of ferroptosis for non-small cell lung cancer therapy. *Chem. Sci.* **14**(34), 9095–9100 (2023). <https://doi.org/10.1039/d3sc01597a>
45. J. Liu, S. Dong, S. Gai, Y. Dong, B. Liu et al., Design and mechanism insight of monodispersed AuCuPt alloy nanozyme with antitumor activity. *ACS Nano* **17**(20), 20402–20423 (2023). <https://doi.org/10.1021/acsnano.3c06833>
46. D. Deng, C. Xu, P. Sun, J. Wu, C. Yan et al., Crystal structure of the human glucose transporter GLUT1. *Nature* **510**(7503), 121–125 (2014). <https://doi.org/10.1038/nature13306>
47. F. Zeng, L. Tang, Q. Zhang, C. Shi, Z. Huang et al., Coordinating the mechanisms of action of ferroptosis and the photothermal effect for cancer theranostics. *Angew. Chem. Int. Ed.* **61**(13), e202112925 (2022). <https://doi.org/10.1002/anie.202112925>
48. K. Li, K. Xu, S. Liu, Y. He, M. Tan et al., All-in-one engineering multifunctional nanoplateforms for sensitizing tumor low-temperature photothermal therapy *in vivo*. *ACS Nano* **17**(20), 20218–20236 (2023). <https://doi.org/10.1021/acsnano.3c05991>
49. B. Xu, S. Li, L. Zheng, Y. Liu, A. Han et al., A bioinspired five-coordinated single-atom iron nanozyme for tumor catalytic therapy. *Adv. Mater.* **34**(15), e2107088 (2022). <https://doi.org/10.1002/adma.202107088>
50. L. Liu, Y. Wu, J. Ye, Q. Fu, L. Su et al., Synthesis of magnesium nanoparticle for NIR-II-photoacoustic-imaging-guided synergistic burst-like and H₂ cancer therapy. *Chem* **8**(11), 2990–3007 (2022). <https://doi.org/10.1016/j.chempr.2022.07.001>

Publisher's Note Springer Nature remains neutral with regard to jurisdictional claims in published maps and institutional affiliations.